



Modelling the forming mechanics of engineering fabrics using a mutually constrained pantographic beam and membrane mesh



Philip Harrison

School of Engineering, University of Glasgow, G12 8QQ, UK

ARTICLE INFO

Article history:

Received 13 October 2015

Received in revised form 31 October 2015

Accepted 2 November 2015

Available online 11 November 2015

Keywords:

A. Fabrics/textiles

B. Mechanical properties

C. Finite element analysis (FEA)

D. Mechanical testing

ABSTRACT

A method of combining 1-d and 2-d structural finite elements to capture the fundamental mechanical properties of engineering fabrics subject to finite strains is introduced. A mutually constrained pantographic beam & membrane mesh is presented and simple homogenisation theory is developed to relate the macro-scale properties of the mesh to the properties of the elements within the mesh. The theory shows that each of the macro-scale properties of the mesh can be independently controlled. An investigation into the performance of the technique is conducted using tensile, cantilever bending and uniaxial bias extension shear simulations. The simulations are first used to verify the accuracy of the homogenisation theory and then used to demonstrate the ability of the modelling approach in accurately predicting the shear force, shear kinematics and out-of-plane wrinkling behaviour of engineering fabrics.

© 2015 The Author. Published by Elsevier Ltd. This is an open access article under the CC BY license (<http://creativecommons.org/licenses/by/4.0/>).

1. Introduction

The large deformation mechanics of biaxial engineering fabrics and viscous advanced composite prepregs are of considerable interest due to the importance of sheet forming processes for the manufacture of advanced composite products and structures. The success or failure in forming a given geometry and the properties of the final composite component are in large part determined by a material's large deformation mechanics and consequently, a significant amount of time and effort has been devoted to characterising and modelling these mechanics with the ultimate aim of predicting and optimising forming processes using virtual design technologies. Six fundamental mechanical properties dominate the deformation of engineering fabrics and advanced composites during forming:

- The tensile properties along the two fibre directions.
- The (trellis) shear resistance of the sheet.
- The out-of-plane flexural modulus of the sheet.
- The in-plane flexural modulus of the sheet.
- The transverse compressive modulus of the sheet.
- The integrity/cohesion of the sheet.

These properties, together with friction, and the boundary conditions applied during the forming process, determine how an engineering fabric or advanced composite will deform and will

influence the generation of unwanted defects. Consequently, an important challenge is in accurately capturing these properties using a suitable combination of constitutive models and modelling techniques to conduct efficient and robust simulations. Equally important are the methods of measuring these properties for real materials; often a time consuming task that can be shortened using multi-scale predictive modelling approaches [1,2]. Generally speaking, the more realistic the modelling approach, the more accurate but computationally expensive the simulation, with longer simulation times reducing the modeller's ability to optimise the forming process. As a result, a compromise is usually made according to the required accuracy, the complexity of the part to be formed and the resources available for computational analysis.

As a first approximation the tensile modulus can be considered as infinite and all other stiffness's of the fabric can be considered negligible; a simplification used in kinematic mapping algorithms [3], allowing fast predictions of draping during forming operations. Nevertheless, accuracy of predictions can be improved by more comprehensive consideration of the forming mechanics. Numerous approaches to modelling biaxial engineering fabrics and viscous advanced composite prepregs during forming have been investigated. Use of continuum elements in modelling relatively thick 3-d fabrics is nowadays computationally tractable and can provide information such as compaction during forming, though long run-times still remain a limiting issue and the approach is less viable for thinner sheets [4]. Instead, constraints on computation speed usually lead to some degree of simplification in order to achieve practical simulation times. This tends to involve the use of

E-mail address: Philip.harrison@glasgow.ac.uk

structural finite elements including truss, beam, membrane, shell elements or some combination of these; each approach brings its own limitations and advantages.

Several viable approaches that ignore out-of-plane bending stiffness and focus on modelling just the tensile and in-plane shear properties of the material have been proposed. For example, use of truss elements to model both fibre and shear resistance allows short run times, though modelling friction with this approach is difficult and requires the use of pragmatic simplifications [5,6]. An alternative is to use membrane elements, here both tensile and shear contributions to the stress are implemented in the element's constitutive law [7–10]. Use of 2-d elements increases simulation times compared to use of 1-d truss elements but potentially allows the implementation of more accurate friction behaviour [11]. When employing 2-d structural elements, careful consideration of the co-ordinate system used to implement the constitutive law is required; the equations must be transformed to the appropriate reference frame used by the finite element code for update of stress and strain using objective derivatives [12,13]. In addition, alignment of mesh and fibre directions is often required to avoid spurious high stresses due to element locking [14] otherwise alternative solutions must be found [15,16]. Yet another approach has been to use 'mutually constrained' elements, using truss elements to represent the fibres and membrane elements to generate in-plane shear resistance [13,17–20]. Here fibre-mesh alignment issues are automatically avoided, though generation of custom meshes is required; a technique that precludes adaptive meshing during the simulation and which may make the application of symmetry conditions more difficult [21]. In all the modelling approaches discussed so far, the formulation of the elements in the mesh means that the elements are freely jointed at their shared nodes. As a result they possess no resistance to out-of-plane bending and compressive stresses can potentially lead to crumpling across the sheet, with the buckling wavelength usually determined by the length of the elements in the mesh. This crumpling can be used to predict the occurrence of in-plane micro-buckles during forming of real-cross ply thermo-plastic laminates [20]. However, in practice, real preforms are able to resist a small amount of compressive stress that stabilises the sheet to some degree. From a pragmatic point of view, early prediction of wrinkles is not necessarily a significant problem and represents a worst-case scenario in predicting real wrinkles in the actual forming processes. However, extensive crumpling of the sheet can lead to excessive element distortion, early failure and lack of robustness of simulations; a more important issue in terms of automated virtual optimisation using the finite element method, e.g. [6,22]. One strategy to avoid this is to delete elements as soon as compressive stresses occur [6], another is to implement negligible compressive stiffness in the truss elements to allow fibre compression rather than buckling [13]. These methods can provide more robust simulations but may obscure some of the detailed predictions of defects, such as micro-buckles and wrinkles.

Introduction of out-of-plane bending stiffness can improve both the realism of wrinkle prediction and the robustness of finite element forming simulations. A simple approach to introducing bending stiffness is to use beam rather than truss elements. Ascough et al. [23] used a square mesh of beam elements to model the draping of clothing fabrics. The formulation of beam elements means that axial and out-of-plane bending stiffness were naturally modelled. Since the beam elements were not freely jointed at shared nodes this inevitably produced in-plane shearing resistance of the sheet due to bending moments between the two fibre directions; resistance unrelated to the fabric's actual shear compliance. Ben Boubaker et al. [24] overcame this issue by connecting the two sets of initially orthogonal beam elements using frictionless hinges. A similar approach was recently adopted in d'Agostino et al. [25],

who modelled a pantographic lattice using beam elements. An alternative modelling strategy to introduce out-of-plane bending stiffness is to use shell elements rather than membrane elements [21,26–30]. This approach can produce realistic wrinkling predictions [30] though the shell element formulation requires significantly greater computation power; Yu et al. [31] reported a 3-fold increase in run time when comparing membrane and shell element-based forming simulations. In an approach designed to permit both trellis shearing and a limited amount of inter-tow sliding, Sidhu et al. [32] combined truss and shell elements; the two sets of tows (initially orientated in orthogonal directions) were indirectly connected via shared shell elements rather than directly with each other. Li et al. [33] also used mutually constrained truss and shell elements to conduct forming simulations; here the elements were directly connected using shared nodes. Later, truss elements were exchanged for beam elements and again the beam and shell elements shared the same nodes; realistic looking wrinkling and forming predictions were reported [34,35]. Combination of continuum and beam elements has also been reported in modelling thick 3-d interlock fabric sheets; beam elements were shown to enhance kinematic predictions in finite element simulations of out-of-plane bending tests [4].

In addition to axial, in-plane shear and out-of-plane bending stiffness, biaxial engineering fabrics and viscous advanced composites also possess an in-plane bending stiffness, with the tows providing resistance to abrupt spatial changes in fibre direction within the plane of the sheet. Relatively little work has been conducted in modelling this property, though awareness of its importance on accurate prediction of fibre direction during forming is growing e.g. [36]. Ferretti et al. [37] used second order continuum theory to predict the gradual rather than abrupt changes in fibre direction observed during actual bias extension tests; augmenting a hyper-elastic energy potential to depend not just on strain but also on the strain gradient. d'Agostino et al. [25] demonstrated the effectiveness of a pantographic beam lattice in reproducing equivalent second-order gradient effects and simultaneously highlighted the limitations of first order continuum approach to modelling fabric mechanics.

The modelling approach used in the current investigation can perhaps best be described as a mutually constrained pantographic beam & membrane mesh. The novelty in the method lies in the manner in which elements are connected and the simple derivation of the homogenised properties of the mesh. The approach is relatively simple and intuitive, and allows independent control of: the axial stiffness along fibre directions, the in-plane shear compliance and both the out-of-plane and in-plane flexural moduli of the sheet. Evaluating the accuracy of a model prior to conducting complex forming simulations is very important for accurate predictions. To do this, methods of identifying the various parameters of the material model and to subsequently evaluate the associated predictions of the model should exist; this can be achieved through the use of simple characterisation tests to isolate the predictions of the model under different deformation modes. This point of view provides the motivation for the current paper and is especially important if additional mechanical properties such as in-plane bending stiffness are introduced in the model.

The structure of the remainder of this paper is as follows: in Section 2 the modelling approach is explained, describing the mutually constrained pantographic beam & membrane mesh in detail. In Section 2.1, simple homogenisation theory is presented, showing how the axial, out-of-plane and in-plane bending stiffness of the sheet are determined from the mesh density, modulus and cross-section of the beam elements (or vice versa). The relationship between average sheet density and the density of the elements in the mesh is also provided. Section 3 is an evaluation of the accuracy of the combined homogenisation/mutually constrained

pantographic beam & membrane mesh under various loading conditions. Conclusions are provided in Section 4.

2. Numerical modelling approach

In previous work using the commercial finite element code Abaqus, e.g. [18–20], mutually constrained truss and membrane elements were combined using shared nodes (see Fig. 1a). Here, the repeat unit cell of the mesh contained a truss element along each side of a square membrane element. Elements were freely jointed at these nodes, resulting in no out-of-plane or in-plane bending stiffness across the sheet. The membrane elements provided the in-plane shear resistance to the sheet using the so-called ‘stress-power model’; the reader is referred to Harrison et al. [38] for further details on this model. The membrane elements also enabled modelling of contact and friction between the sheet and tooling. Any of the friction behaviours available in Abaqus can be employed or custom friction behaviour can be implemented using a VFRIC user subroutine. The idea behind the current investigation is to examine the use of beam rather than truss elements in modelling the role of the fibres in the material. The standard formulation of beam elements means that, not just axial stiffness, but also out-of-plane and in-plane bending resistance can be modelled. However, simply replacing the truss elements with beam elements leads to the introduction of bending moments during trellis shear of the mesh; shared nodes no longer act as freely jointed connections between the two, initially orthogonal sets of beam elements. To eliminate these bending moments the mesh structure shown in Fig. 1b is used. Here, one set of Timoshenko beam elements (type B31) lies a very small distance above the membrane elements (type M3D4R), the other initially orthogonal set of beam elements lies at an equal distance below the membrane elements. The corner nodes of the membrane element are connected to either end of the beam elements via zero torque hinge connector elements (available in the Abaqus library) [39]. The hinge elements constrain the relative position of the nodes but allow free rotation between the beam elements. An in-house Matlab™ code, Varifab [40], has been modified in order to automatically generate the mesh in a format compatible with Abaqus input files.

2.1. Homogenised mechanical stiffness and density of the sheet

In this section, equations relating the homogenised tensile and flexural properties of a rectangular sheet, measuring L metres long and W metres wide, to the mechanical properties, dimensions and density of the beam and membrane elements of the mesh used to model the sheet, are derived. L and W are integer multiples of l_B , the length of the beam elements in the mesh. The length of beam elements and equally, the side length of the membrane elements are decided when generating the mesh for the simulation and depend on issues such as the curvature of the geometry to be

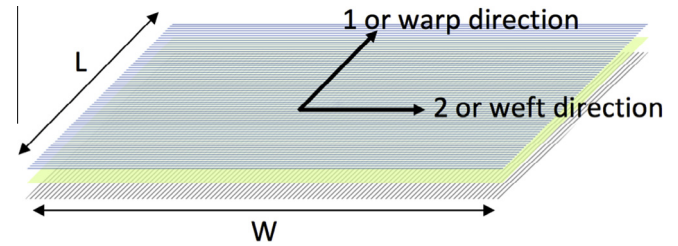


Fig. 2. Rectangular mesh of mutually constrained pantographic beam & membrane elements of width, W , and length, L , showing the 2 independent, initially perpendicular fibre directions positioned above and below the membrane elements. The 2 fibre directions are indicated in the figure. (For interpretation of the references to colour in this figure legend, the reader is referred to the web version of this article.)

modelled. Abaqus provides considerable scope to include nonlinear beam section behaviour [39]; the current work represents a first step in the development of this alternative modelling approach and is limited to the case of linear elastic material behaviour. A Timoshenko beam formulation was employed, using a prismatic rectangular cross section with an effective Poisson’s ratio of 0. The beam transverse shear stiffness was determined using the default method discussed in the Abaqus documentation (see Section 29.3.3 of [39]). Note that Euler–Bernoulli beams are not available in Abaqus Explicit, though the effect of shear considered by the Timoshenko beam element formulation can be neglected when the beam length is very much greater than its cross-section dimension, as is the case throughout this investigation. Beam section properties are recomputed during the progression of the simulation. The beam elements are capable of undergoing finite axial deformations if required. The following homogenisation analysis assumes that the mechanical properties in the two fibre directions (here 1 and 2 directions for cross ply laminates or warp and weft directions for woven fabrics – see Fig. 2) are not necessarily the same, i.e. the sheet properties can be unbalanced.

2.1.1. Axial properties of mesh

Due to the uncertainty in the thickness, t_s , of compressible fabrics during testing, data is sometimes plotted as force per unit side length, N , versus strain, rather than stress versus strain, e.g. [5]. The gradient of such experimental tensile test data is $E_s t_s$, i.e. the sheet’s tensile stiffness multiplied by its thickness, referred to here as the ‘line stiffness’, γ , and can be a convenient property to use when modelling textiles. γ is easily measured experimentally and can be used to assign realistic properties in numerical simulations. In order to represent a given material, meshes of different mesh densities must have the same value of γ , i.e. two meshes of equal side length must produce the same tensile force, F , when stretched to the same tensile strain, ϵ . To achieve this for the mutually constrained pantographic beam & membrane mesh

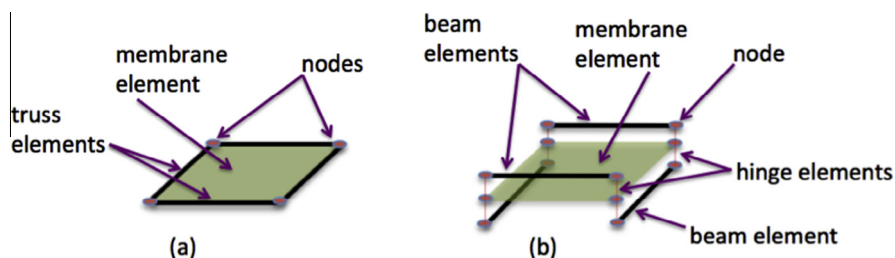


Fig. 1. Repeat unit cells. (a) Mutually constrained truss and membrane elements, (b) mutually constrained pantographic beam & membrane mesh used in the current investigation, connections are provided by zero-torque hinge elements. (For interpretation of the references to colour in this figure legend, the reader is referred to the web version of this article.)

shown in Fig. 1b, the beam modulus, E_B , cross-sectional area and mesh density must be considered, i.e.

$$F = E_{B1} A_{T1} \varepsilon \quad (1)$$

where the subscript, B1, indicates the parameter is associated with the beam elements orientated in the 1 (or warp) direction in the mesh, see Fig. 2. A_{T1} is the total sum of the cross-sectional areas of all beams in the mesh measured across the width of the sheet, W , in the plane perpendicular to the direction of stretching. Assuming that mesh contains prismatic beam elements of rectangular cross-sectional area, A_{B1} , then

$$A_{B1} = w_{B1} t_{B1} \quad (2)$$

where w_{B1} and t_{B1} are the width and thickness of the beam element cross-section corresponding to elements orientated in the 1 direction in a given mesh, then the total beam cross section, A_{T1} , in a mesh of width, W is

$$A_{T1} = w_{B1} t_{B1} \left\{ \frac{W + l_B}{l_B} \right\} \quad (3)$$

where l_B is the length of each beam element in the mesh (which is the same in the 1 and 2 directions) and characterises the mesh density. From Eqs. (1) and (3), the force per unit side length in the 1 direction, N_1 , in a given mesh is given as

$$N_1 = E_{B1} w_{B1} t_{B1} \left\{ \frac{W + l_B}{W l_B} \right\} \varepsilon \quad (4)$$

and therefore, the line stiffness in the 1 direction is

$$\gamma_1 = E_{B1} w_{B1} t_{B1} \left\{ \frac{W + l_B}{W l_B} \right\} \quad (5)$$

a similar expression can be written for the 2 direction by changing the subscript 1 for 2 and changing W to L . The same is true for the equations in Sections 2.1.2 and 2.1.3.

2.1.2. Out-of-plane flexural modulus of mesh

Similar arguments can be used to calculate the out-of-plane bending stiffness of the mesh with respect to the axis of the two fibre directions. Their very high slenderness ratio means the beams can be treated using Euler Bernoulli theory. Assuming the beam lies with its width in the plane of the sheet, the out-of-plane flexural modulus per unit width of a mesh of beam elements is just the sum of the flexural modulus of each beam in the mesh in a given direction [41]. Thus, for the 1 direction (see Fig. 2) this is

$$\beta_1 = \frac{E_{B1} w_{B1} t_{B1}^3}{12} \left\{ \frac{W + l_B}{W l_B} \right\} \quad (6)$$

2.1.3. In-plane flexural modulus of mesh

The in-plane bending modulus per unit width of the mesh is found in the same way. Again the in-plane flexural modulus per unit side length of a mesh of beam elements is just the sum of the flexural modulus of each beam in the mesh. Thus, for the 1 direction (see Fig. 2) this is

$$\alpha_1 = \frac{E_{B1} w_{B1}^3 t_{B1}}{12} \left\{ \frac{W + l_B}{W l_B} \right\} \quad (7)$$

In this case, the width rather than the thickness of the beam elements has the greater influence on the in-plane bending modulus.

2.1.4. Determining the beam element properties from mesh properties

Eqs. (5–7) are three independent equations that relate the homogenised macro-scale axial and bending properties of the mesh to the modulus and dimensions of the beam elements in the mesh. If a sheet of a given mesh density is created then l_B is

known and E_B , w_B and t_B can be uniquely determined from the desired macro-scale properties of the sheet, from Eq. (5),

$$E_{B1} = \frac{\gamma_1 W l_B}{w_{B1} t_{B1} (W + l_B)} \quad (8)$$

Substitute Eqs. (8) in (6) to find

$$t_{B1} = \sqrt{\frac{12 \beta_1}{\gamma_1}} \quad (9)$$

likewise, substitute Eq. (8) in Eq. (7) to find,

$$w_{B1} = \sqrt{\frac{12 \alpha_1}{\gamma_1}} \quad (10)$$

Finally, substitute Eqs. (9) and (10) back in Eq. (8) to find,

$$E_{B1} = \frac{\gamma_1^2 W l_B}{12 (W + l_B) \sqrt{\alpha_1 \beta_1}} \quad (11)$$

Thus, for a given element length, l_B , and sheet side length, W , Eqs. (9–11) uniquely relate the beam modulus and cross-section to the measurable homogenised macro-scale sheet properties in the 1 direction, α_1 , β_1 and γ_1 . As stated earlier, equivalent properties can be found for the 2 direction using simple substitutions.

2.1.5. Relating element density and sheet density

When conducting dynamic explicit finite element simulations, if material damping is ignored and considering beam and membrane elements a non-conservative (see Section 6.3.3 of [39]) estimate of the maximum stable time increment, Δt , calculated on an element-by-element basis for isotropic linear elastic material behaviour with a Poisson's ratio of 0, is given by,

$$\Delta t = L_e \sqrt{\frac{\rho_e}{E_e}} \quad (12)$$

where L_e is the characteristic length of elements in the mesh, ρ_e is the material density assigned to the element and E_e is the modulus of the material assigned to the element [39]. Consequently, for a given mesh density, faster simulations can be run by maximising the ratio ρ_e/E_e through the use of mass-scaling, i.e. the density can be artificially increased. If mass scaling is used, care should be taken to avoid the introduction of unintended inertial effects. Further restrictions apply when gravity is modelled. This imposes an upper limit to the density of the elements in the mesh. It can be shown that the average volumetric density, ρ_a , of the mutually constrained membrane and beams elements within the mesh can be calculated using

$$\rho_a = \rho_{areal} \left\{ \frac{l_B W L}{L w_{B1} t_{B1} (W + l_B) + W w_{B2} t_{B2} (L + l_B) + t_m l_B W L} \right\} \quad (13)$$

where ρ_{areal} is the sheet's areal density and t_m is the thickness of the membrane elements. Both of these parameters can be measured from the fabric sheet. Note; the thickness of the membrane elements has no influence on the flexural properties of the mutually constrained pantographic beam & membrane mesh. If the density of the beam elements is considered equal along the two fibre directions then

$$\rho_B = \frac{\rho_a \%_B}{100} \cdot \left\{ \frac{t_m W L l_B + w_{B1} t_{B1} (W + l_B) L + w_{B2} t_{B2} (L + l_B) W}{w_{B1} t_{B1} (W + l_B) L + w_{B2} t_{B2} (L + l_B) W} \right\} \quad (14)$$

where $\%_B$ is the percentage of the total mass of the mesh, residing in the beam elements. The stiffest elements in the mesh are the beam elements; these represent the high modulus fibre contribution. Consequently, the beam elements rather than the membrane elements impose the largest restriction on the maximum stable time increment given by Eq. (12) and so, in order to maximise simulation

speed, $\%_B$ should be chosen relatively large, for example, at 90%. Using Eq. (14), the density of the membrane elements, ρ_m , is

$$\rho_m = \frac{\rho_B}{l_B t_m W L} \cdot [w_{B1} t_{B1} (W + l_B) L + w_{B2} t_{B2} (L + l_B) W] \cdot \left(\frac{100}{\%_B} - 1 \right) \quad (15)$$

The sheet dimensions are decided when setting up the simulation. Once the element length is chosen, dimensions of the beam element cross section are automatically provided by Eqs. (9) and (10) in order to produce the desired mechanical response. The initial thickness of the membrane elements is chosen to correspond with the initial thickness of the sheet.

3. Numerical and theoretical evaluation

The axial and out-of-plane flexural behaviour of the mutually constrained pantographic beam & membrane mesh are first examined in Sections 3.1 and 3.2; results are used to verify the homogenisation theory presented in Section 2. Simulations of a uniaxial bias extension test are presented in Section 3.3. The influence of shear compliance, in-plane and out-of-plane flexural rigidity on both kinematic predictions and wrinkling behaviour of the test specimen is then examined and the implications of the findings are considered.

3.1. Investigating the tensile response of the mutually constrained pantographic beam & membrane mesh

Woven textiles usually show a strongly coupled, non-linear bi-axial tensile behaviour that is difficult to measure and model accurately [42–44]. Consequently, the method proposed here can provide only a first approximation of the tensile properties of woven fabrics and is a limitation of the method. Use of linear beam elements means the approach is better suited to modelling linear tensile behaviour in the fibre directions, more appropriate for cross-ply laminates or non-crimp stitched fabrics. The tensile response of the mutually constrained pantographic beam & membrane mesh is evaluated here. To do this, an approximate tensile modulus of the sheet, E_s , acting along the two fibre directions of a balanced biaxial sheet is estimated using,

$$E_s = \frac{E_{\text{fibre}} \cdot f}{2} \quad (16)$$

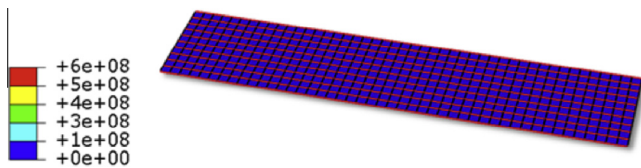


Fig. 3. Tensile test showing Von Mises stress (in Pa), the stress is concentrated in the beam elements orientated along the length direction of test specimen (the loading direction). (For interpretation of the references to colour in this figure legend, the reader is referred to the web version of this article.)

where f is the fibre volume fraction of the sheet. Assuming a S-glass fibre modulus of 86 GPa and a fibre volume fraction of 0.6, a sheet modulus of 26 GPa is obtained and if a sheet thickness of 0.5 mm is assumed, this produces a line stiffness, γ , of $1.3 \times 10^6 \text{ N m}^{-1}$. A simulation of a tensile test (Case 1A) has been performed on a strip, measuring $115 \times 25 \text{ mm}$, to examine the accuracy of Eqs. (5–11). A beam element length of 0.0025 m was employed in creating the mesh, see Fig. 3. Realistic values for the bending rigidities have been assigned (see Tables 1 and 2). In practice the bending rigidity of the mesh should have no influence on the tensile response of the strip. However, according to the homogenisation theory of Section 2, the beam modulus and cross section are influenced by the bending properties and so the tensile simulation effectively evaluates the full homogenisation theory for the mechanical properties of the mesh (but not the physical density of the mesh). A fabric-specific constitutive equation is used in the membrane elements to model shear compliance, though this has a negligible tensile stiffness and therefore contributes very little to the reaction force [38]. The mesh was held fixed at one end and stretched by 1.15 mm (1% strain). The total reaction force measured at the free end of the strip was plotted versus engineering strain, the gradient of the resulting curve is the line stiffness of the sheet and the simulation produced a value of $1,293,228 \text{ N m}^{-1}$, a relative difference of about 0.5% with the input value used to determine the modulus and cross section of the beam elements used in the mutually constrained pantographic beam & membrane mesh. This simple simulation effectively verifies the mechanical homogenisation equations presented in Section 2.

3.2. Investigating the out-of-plane flexural response of the mutually constrained pantographic beam & membrane mesh

The bending behaviour of clothing fabrics is well studied, e.g. [45]. Investigations into the bending response of composite reinforcements are closely related and often use many of the same experimental techniques to determine mechanical properties. Reports have been published on the out-of-plane flexural modulus of viscous prepregs [46], woven engineering fabrics [21,31,47], non-crimp fabrics [31,34,48] and 3-d interlock fabrics [4] using a variety of test methods; see [47] for a comprehensive review. The flexural modulus per unit width of woven, non-crimp and 3-d interlock fabrics is rate-independent; representative values can be found in the literature and are summarised in Table 2.

Table 2
Examples of out-of-plane flexural moduli per unit width reported in the literature.

Fabric	Approx. initial fabric thickness (mm)	Reference	Value ($\text{N m}^2 \text{ m}^{-1}$)
Quadri-axial carbon NCF	1.4	[48]	0.018
Bi-axial carbon NCF	1.2	[48]	0.0075
Bi-axial carbon NCF	0.85	[48]	0.020
2.5D carbon fabric	1.0	[47]	0.00449–0.00678
Interlock carbon fabric	0.6	[47]	0.00616–0.00884
Plain woven glass/PP	0.5	[31]	0.0137

Table 1

Sample dimensions, macro-scale axial and flexural properties input for dynamic explicit simulations using mutually constrained pantographic membrane and beam mesh for tensile simulation.

Case	Strip length (mm)	Strip width (mm)	Line stiffness m^{-1} in warp (left) and weft (right) directions (N m^{-1})	Out-of-plane rigidity m^{-1} in warp (left) and weft (right) directions ($\text{N m}^2 \text{ m}^{-1}$)	In-Plane rigidity m^{-1} in warp (left) and weft (right) directions ($\text{N m}^2 \text{ m}^{-1}$)	Areal density (kg m^{-2})
1A	115.0	25	1.3×10^6 1.3×10^6	0.02 0.02	0.02 0.02	1.0

Values from [48] in Table 2 correspond to low curvatures; the stiffness was reported to drop by a factor of about 10 times when tested to higher curvatures. Non-linear behaviour has also been reported by, for example, [31,47] and so it should be noted that values in Table 2 are most likely subject to significant change depending on the fabric curvature.

The British Standard (BS EN ISO 9073-7:1998) [49] for measuring the out-of-plane bending stiffness of fabrics is a simple cantilever test. The test is used in this investigation to evaluate the predictions of dynamic explicit simulations produced using the mutually constrained pantographic beam & membrane mesh. The main equation of the standard is based on a truncated power series solution to the system's governing second order differential equation, provided by Peirce [52],

$$G_{pe} = \frac{1}{\frac{\tan\phi}{\cos(0.5\phi)}} \times \frac{pL_s^3}{8} \quad (17)$$

where G_{pe} is the flexural rigidity (per unit width), ϕ is the angular deflection of the cantilever end (see Fig. 4), p is the mass per unit area multiplied by the acceleration due to gravity, taken here to be 9.81 ms^{-2} and L_s is the cantilever strip length. However, inaccuracies in the predictions of this equation were recently discussed by Lammens et al. [50] and Plaut [51], the latter suggested an enhanced formula over Eq. (17), valid for general cases, given in the form of a 5th order polynomial equation.

In the current investigation, an accurate benchmark equation to assess predictions of the mutually constrained pantographic beam & membrane mesh and associated homogenisation theory, over a wide range of bending deflections is required. To this end, static implicit finite element simulations of a cantilever test have been performed using linear shell elements (S4R) with the commercial finite element code, Abaqus Standard. Transverse shear properties of the shell elements were calculated using the default method used by Abaqus (see Section 29.6.4 of [39]). A Poisson's ratio of just 0.05 was used in the linear elastic material model to mitigate stiffening of the cantilever strip due to anticlastic curvature [50]. Twenty different cases (Cases 1B–20B) were simulated using a range of parameters (see Table A1 for details). In each case the flexural rigidity per unit width of the strip, Eq. (18), employed in the finite element simulations was given as

$$G_{EB} = \frac{Eh^3}{12} \quad (18)$$

where G_{EB} is the flexural modulus per unit width according to Euler–Bernoulli assumptions, E is the Young's modulus of the shell elements, h is the thickness of the strip. Note that shear effects considered by the shell elements in Abaqus Standard can be neglected

when the thickness is small compared to the length of the cantilever beam, as is the case in this investigation, and so convergence on Euler–Bernoulli type behaviour is to be expected. Results of these numerical simulations suggested an empirical correction to Eq. (17) that can be expressed as

$$G_C = G_{pe} \cdot f(\phi) = \frac{f(\phi)}{\frac{\tan\phi}{\cos(0.5\phi)}} \times \frac{pL_s^3}{8} \quad (19)$$

where

$$f(\phi) = (-3.2434387343 \times 10^{-5}) \cdot \phi^2 + (3.8717591439 \times 10^{-6}) \cdot \phi + 0.9988589066$$

Although the formulation of Eq. (19) is based purely on empirical fitting to a limited selection of cases, the extremely high regression coefficient in determining $f(\phi)$ suggests the result can be generally applied. Plotting the ratio between flexural modulus per unit width used in finite element simulations (Eq. (18)) and the various approximations of this property (i.e. linear theory [41], Eq. (17) from Peirce, the approximation given by Plaut [51], and also Eq. (19)) in Fig. 5 provides a convenient visual means of assessing the accuracy of each these approximations. Eq. (19) was found to give excellent agreement with both the enhanced equation provided by Plaut for large values of ϕ ($>5^\circ$), where analytical linear theory [41] is inaccurate, and also excellent agreement with analytical linear theory for low values of ϕ ($<5^\circ$), where the predictions by Plaut [51] were found to be less reliable (see Fig. 5) (though this inaccuracy is presumably simply related to

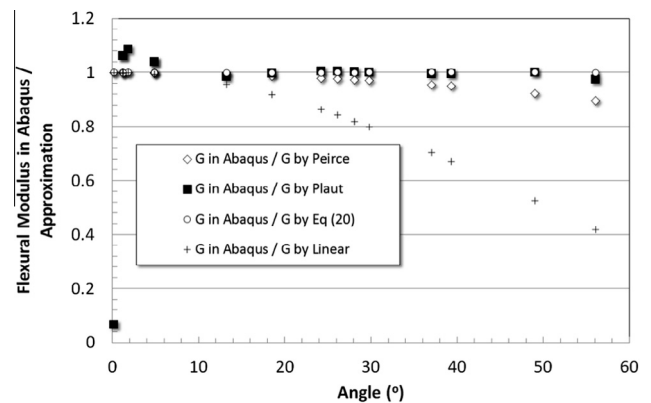


Fig. 5. Comparison of ratio between flexural modulus per unit width used in finite element simulations and the approximation of this property using a linear solution, the approximation made by Peirce [52] and that made by Plaut [51].

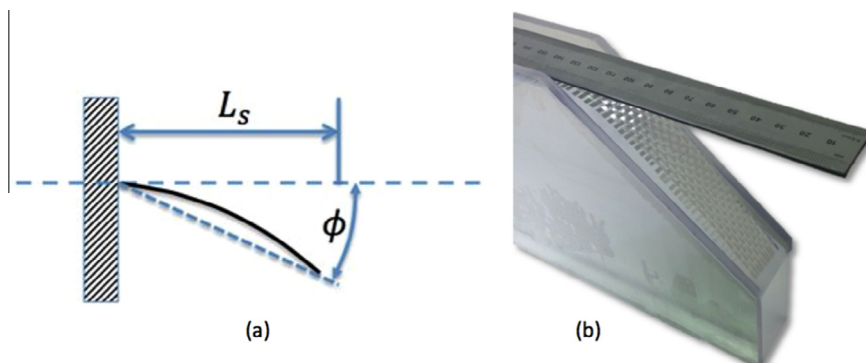


Fig. 4. (a) Parameters of cantilever bend test and (b) photograph of typical test setup. (For interpretation of the references to colour in this figure legend, the reader is referred to the web version of this article.)

Table 3

Sample dimensions, macro-scale axial and flexural properties input for dynamic explicit simulations using mutually constrained pantographic beam & membrane mesh.

Case number	Strip length (mm)	Strip width (mm)	Line stiffness m^{-1} in warp (left) and weft (right) directions ($N m^{-1}$)		Out-of-plane rigidity m^{-1} in warp (left) and weft (right) directions ($N m^2 m^{-1}$)		In-plane rigidity m^{-1} in warp (left) and weft (right) directions ($N m^2 m^{-1}$)		Areal density ($kg m^{-2}$)	Run time (min)
1C	115.0	25	6000	6000	0.0005	0.0005	0.0005	0.0005	0.700	15.0
2C	115.0	25	6000	6000	0.0005	0.0005	0.05	0.05	0.700	83.0
3C	115.0	25	6000	6000	0.0005	0.001	0.0005	0.001	0.700	18.0
4C	115.0	25	10,000	10,000	0.005	0.005	0.005	0.005	0.5	18.0
5C	115.0	25	10,000	10,000	0.005	0.005	0.005	0.005	0.5	35.0

the number of significant figures given for the polynomial coefficients provided in [51]). Eq. (19) was therefore used as the benchmark with which to evaluate predictions of the mutually constrained pantographic beam & membrane mesh. Note; Appendix A explains why the British Standard, which involves the use of Eq. (17), remains a reasonably accurate test method and can still be employed to provide an approximate single value of the out-of-plane bending modulus without modification, when characterising textiles. However, it is worth mentioning that more precise modelling of the actual non-linear bending behaviour of fabrics could probably be introduced through appropriate manipulation of the shear modulus of the Timoshenko beam elements. In this case, more accurate measurement of the flexural modulus would be required to identify the non-linear bending behaviour, e.g. [47]. For the purpose of this preliminary investigation, which is restricted to linear bending behaviour, just a single value for the flexural modulus of the sheet is sufficient.

Five arbitrary test cases (Cases 1C–5C) were used to evaluate the predictions of the mutually constrained pantographic beam & membrane mesh. In order to conduct the dynamic simulations using this approach, viscous damping was added to simulations using mass-proportional Rayleigh damping to mitigate oscillations of the cantilever strip; a coefficient of $30 s^{-1}$ was used (see Section 26.1.1 of [39]). A mutually constrained pantographic beam & membrane mesh was generated; the dimensions of the strip are given in Table 3, together with areal density and macro-scale axial and flexural properties. The simulation time is also provided (computer specification: Intel Core i7-3770 CPU@3.40 GHz; 16.0 GB, 64-bit OS). In all cases, the side length of the square membrane elements was 0.0025 m and the thickness of the

membrane elements was 0.002 m (see Fig. 6). The modulus and cross section of beam elements, and the density of beam and membrane elements were calculated from the macro-scale properties using the equations presented in Section 2 and the areal density of the sheet (see Section 2.1.5). Note that while tensile, shear and in-plane properties are required inputs for these simulations, they can all be provided as arbitrary values as only the out-of-plane rigidity in the direction of the long axis of the strip, the length of the strip and the areal density of the strip determine the final angular deflection.

In Cases 1C and 2C, balanced mesh properties were used and membrane elements were given isotropic linear elastic properties with a very low modulus of 1 kPa. In Case 1C the out-of-plane and in-plane flexural moduli were equal (the run time of equivalent static implicit simulations was around 7.5 times faster). In Case 2C, the in-plane modulus was increased by a factor of 100 compared to Case 1C, demonstrating the independent control of the out-of-plane and in-plane flexural moduli of the mesh (though it is highly unlikely that such a large difference would exist in real fabrics). Different values for the out-of-plane and in-plane flexural moduli led to higher run times, perhaps attributable to an increase in the highest frequency mode of the beam elements which could change the fraction of critical damping in the highest frequency mode, leading to a reduction in Δt ; see Section 26.1.1 of [39]. In Case 3C unbalanced properties were used, the flexural modulus in the direction of the width of the strip was $2\times$ higher than in the length direction. Case 4C examined the predictions for a stiffer and lighter sheet while Case 5C examined the change in computational resource when using a fabric-specific constitutive model in the membrane elements. Results given in Table 4 demonstrate that, according to Eq. (19), the angular deflection of the strip predicted by the simulations correlates very well with the out-of-plane bending rigidity input in the simulations. Predictions were generally within a few per cent of the input value irrespective of the in-plane modulus used in the simulation. The predictions verify the accuracy of the homogenisation equations presented in Section 2 and also suggest the computation cost is generally insensitive to the flexural properties assigned to the sheet unless the ratio between in-plane and out-of plane bending stiffness is extreme. As expected, use of the fabric-specific model has an extra computational cost compared to a simple linear elastic model.

3.3. Investigating the shear and in-plane bending response of the mutually constrained pantographic beam & membrane mesh

The uniaxial bias extension test is commonly used to investigate the shear stiffness of rate-independent engineering fabrics and rate-dependent prepreps, e.g. [5,6,9,10,14,53]. More recently, the same test has been used to highlight the important influence that a fabric's in-plane bending stiffness has on a specimen's in-plane deformation kinematics [25,36,37,55]. In this section, it is shown that the both the shear stiffness and in-plane bending

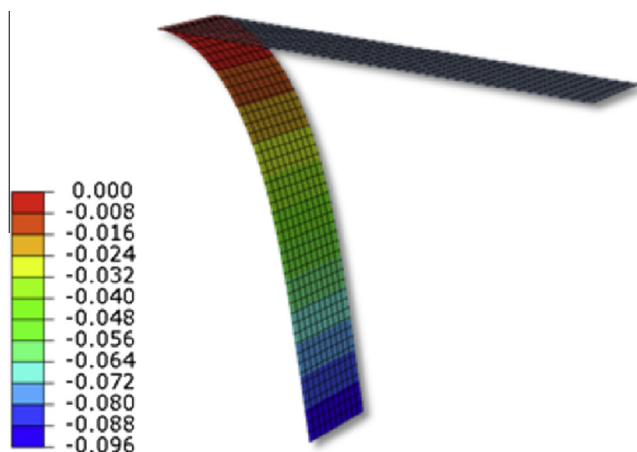


Fig. 6. Undeformed and deformed cantilever strip from case 1 (see Table 4), the colour legend indicates the z-component of displacement from the original position (in m). (For interpretation of the references to colour in this figure legend, the reader is referred to the web version of this article.)

Table 4
Simulation predictions corresponding to input parameters of Table 3.

Case Number	Angular deflection (°)	Out-of-plane rigidity m^{-1} from Eq. (19) ($N m^2 m^{-1}$)	Notes
1C	62.7	0.000503	Linear elastic in membrane elements
2C	62.4	0.000485	Linear elastic in membrane elements
3C	63.0	0.000494	Linear elastic in membrane elements
4C	10.8	0.00485	Linear elastic in membrane elements
5C	10.5	0.00498	Vumat in membrane elements

stiffness work together to simultaneously determine the measured axial force and the observed in-plane deformation kinematics of the uniaxial bias extension test specimen.

All simulations of the uniaxial bias extension test reported in Sections 3.3 (and Section 3.4) employed certain common properties. The finite element mesh measured 199.4 mm high (H) and 97.6 mm wide (W), thus the aspect ratio, λ , was 2.044. The truss element length was 3 mm. An ‘encastre’ boundary condition was applied to all nodes in Region C1, while a y -displacement of 42 mm was applied to all nodes in Region C2 (see Fig. 7a for

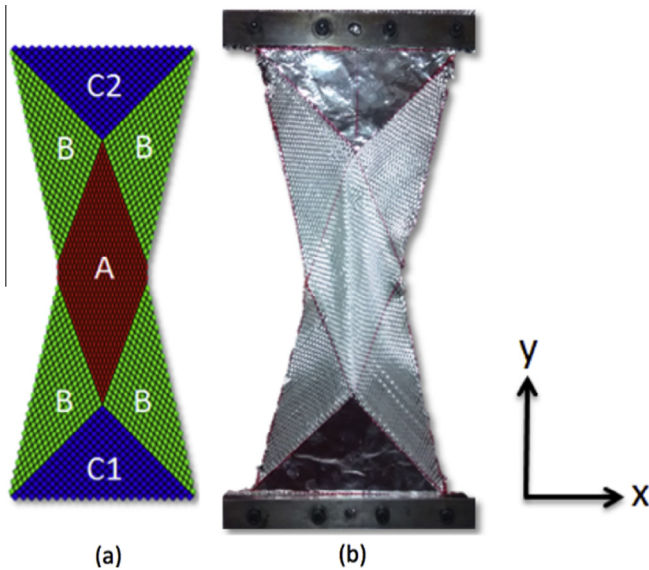


Fig. 7. Boundary conditions imposed in the simulations of this investigation are equivalent to bonding aluminium foil in Region C1 and C2 in actual experiments. (For interpretation of the references to colour in this figure legend, the reader is referred to the web version of this article.)

Table 5
Mechanical properties of the sheet.

Case number	Tensile stiffness in fibre directions (GPa)	Shear force vs shear angle input curve ($N m^{-1}$)	In-plane bending modulus ($N m^2 m^{-1}$)	Out-of-plane bending modulus ($N m^2 m^{-1}$)	Run time (h)
1D	2.5	$F_{sh}(\theta) = 0.1\theta$	0	0	11.5
2D	0.25	$F_{sh}(\theta) = 0.1\theta$	0.001	0.001	17.0
3D	0.25	$F_{sh}(\theta) = \theta$	0.001	0.001	17.0
4D	0.25	$F_{sh}(\theta) = 0.204204653\theta - 0.0380457956\theta^2 + 0.0042508987\theta^3 - 0.0001706295\theta^4 + 0.0000024329\theta^5$	0.001	0.001	14.2
5D	0.25	Same as 4D	0.001	0.002	
6D	0.25	Same as 4D	0.002	0.001	

labelled regions), all other displacements and rotations were zero. This boundary condition eliminates any unwanted deformation in Region C [54,60]. An equivalent condition can be imposed experimentally by bonding aluminium foil across these regions prior to testing (effectively creating a rigid composite material, see for example, Fig. 7b). An areal density of $1.5 kg m^{-2}$ was applied with 90% of the mass residing in the 1-d elements (truss or beam). The membrane elements had a thickness of 0.5 mm. Other homogenised mechanical properties, including the tensile stiffness along the fibre directions, shear stiffness of the sheet and the in-plane and out-of-plane bending stiffness are case-specific and are listed in Table 5. The approximate simulation run-time of each simulation is also provided.

The objective of the first simulation (Case 1D) was to evaluate the simulation predictions in the absence of any in-plane or out-of-plane flexural stiffness. To this end, the mutually constrained truss and membrane approach was used (see Fig. 2a). A simple linear shear force per unit length versus shear angle behaviour was input, i.e.

$$F_{sh}(\theta) = 0.1\theta \quad (20)$$

where θ is the shear angle in the material. The homogenised tensile modulus in the fibre directions was set at 2.5 GPa. Fig. 8a–c show the shear angle across the deformed mesh at 3 different displacements (12.6, 25.2 & 37.8 mm). The three distinct regions of the test specimen, Regions A–C, (see Fig. 7a) are evident. The lack of in-plane bending stiffness means that the shear angle can undergo an abrupt change between the three regions without creating any contribution to the strain energy of the sheet. In Fig. 9, the kinematics are examined further by plotting of the shear angle predicted in an element near the centre of Region A, θ_e , against the theoretical shear angle predicted from ideal kinematics, using Eq. (21)

$$\theta_t = \frac{\pi}{2} - 2a \cos \left\{ \frac{Wd}{\sqrt{2}(\lambda - 1)} + \frac{1}{\sqrt{2}} \right\} \quad (21)$$

where θ_t is the theoretical shear angle in Region A of the test specimen and d is the displacement applied to the top of the test specimen. As expected the shear angle in the central element, θ_e (red line), closely follows ideal kinematics (dashed black line).

The theoretical axial force measured in the uniaxial bias extension test, F_{be} , can be predicted using normalisation theory for rate-independent fabrics. Two such theories have been independently derived [56,57], the resulting normalisation equations of both theories can be shown to be exactly equivalent [58] (a finding contrary to the erroneous conclusion of [59]). Following [58] the theoretical axial force can be predicted by incorporating the input shear force curve, Eq. (20) in Eq. (22).

$$F_{be}(\theta_t) = \frac{\sqrt{2} \cdot W}{(\lambda - 1)} \left\{ \begin{array}{l} F_{sh}(\theta_t) \cdot (2\lambda - 3) \cdot \cos\left(\frac{\pi}{4} - \frac{\theta_t}{2}\right) + \\ F_{sh}(\theta_t/2) \frac{\sin(\pi/4 - \theta_t/4)}{\sin(\pi/4 - \theta_t/2)} \cdot \cos\left(\frac{\pi}{4} - \frac{\theta_t}{4}\right) \end{array} \right\} \quad (22)$$

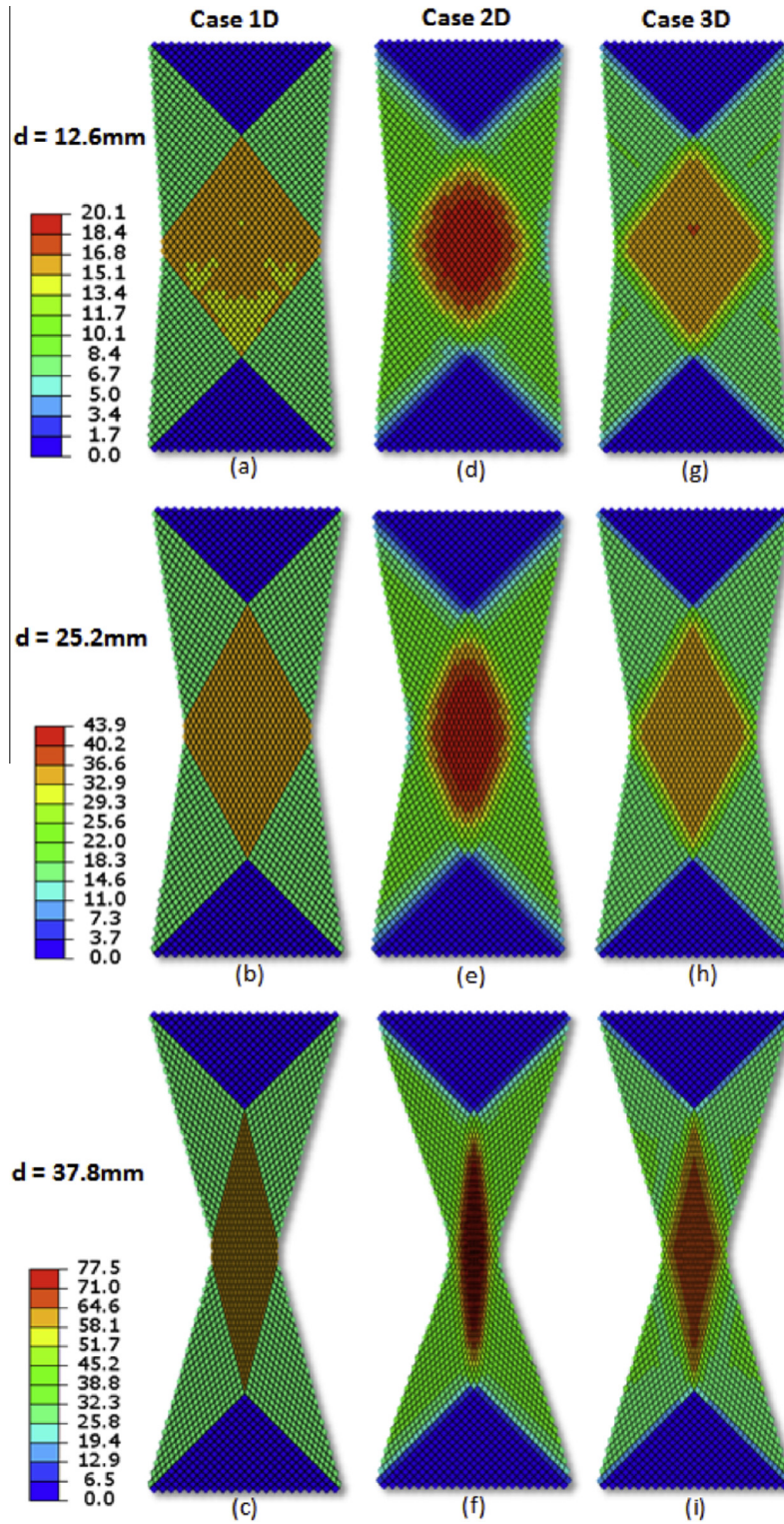


Fig. 8. Three simulations of the uniaxial bias extension test. (a–c) Case 1D involves zero flexural stiffness and low shear force, (d–f) Case 2D is the same as 1D but with added in-plane and out-of-plane flexural stiffness (g–i) Case 3D is the same as Case 2D but with 10× higher shear stiffness. (For interpretation of the references to colour in this figure legend, the reader is referred to the web version of this article.)

The ideal axial force result is shown in Fig. 10a (black dashed line) together with the axial reaction force predicted by the simulation (red line). Very good correspondence is found, effectively verifying the accuracy of the membrane elements and stress-power model in representing the shear stiffness of the fabric to

very high shear angles. Note that reducing the tensile stiffness in the fibre directions tends to lower the shear angle prediction below the ideal case.

In Case 2D, flexural stiffness was introduced by switching to the mutually constrained pantographic beam & membrane mesh (see

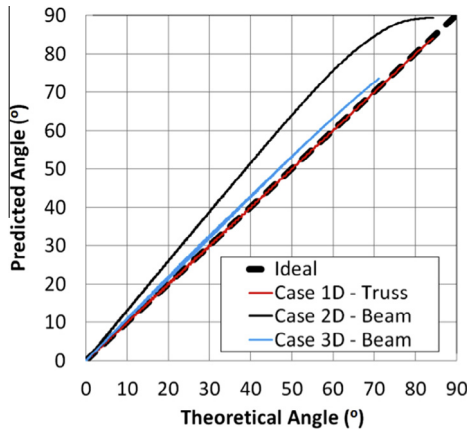


Fig. 9. Shear angle predicted at the centre of Region A versus the ideal theoretical shear angle predicted using Eq. (21) for Cases 1D, 2D and 3D. (For interpretation of the references to colour in this figure legend, the reader is referred to the web version of this article.)

Fig. 2b). A value of 0.001 N mm^{-1} was used for both the in-plane and out-of-plane bending stiffness. Eq. (20) was again used for the shear stiffness. The full field shear angle prediction is shown in Fig. 8d–f and clearly demonstrates the important influence that the in-plane bending stiffness has on predictions of the shear kinematics across the sheet; the strain energy contribution due to

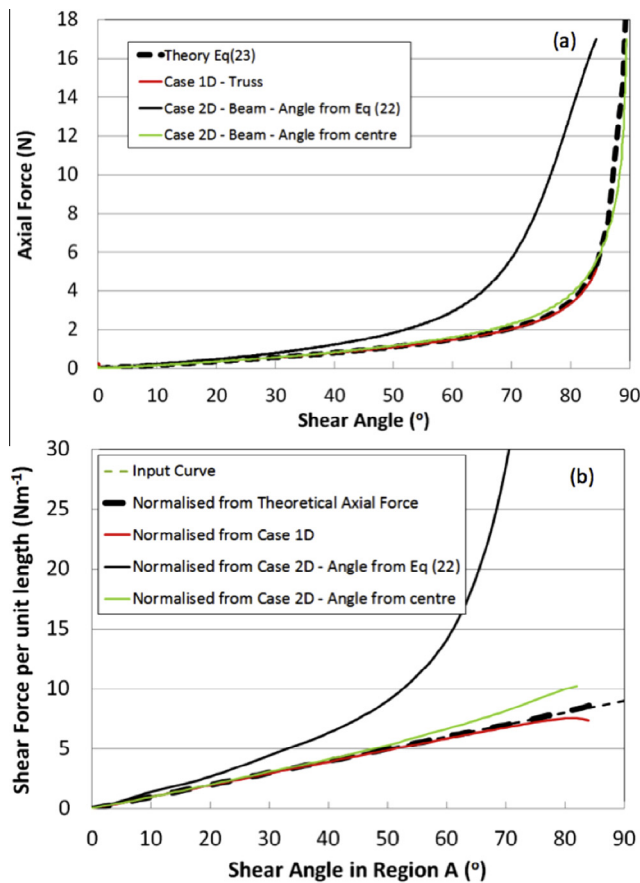


Fig. 10. (a) Axial reaction force predictions from Eq. (22), Case 1D and Case 2D. The axial force of Case 2D is plotted against the shear angle determined both using Eq. (21) and predicted from an element at the centre of Region A. (b) Normalised shear force per unit length versus shear angle curves obtained using the four axial force curves shown in (a). (For interpretation of the references to colour in this figure legend, the reader is referred to the web version of this article.)

bending of the fibres causes a more gradual change in the shear angle between the 3 regions; similar results were reported recently in [25,36,37,55]. Shear angle predictions, θ_e , at the centre of Region A are again plotted in Fig. 9 and show a significant increase over ideal kinematics (continuous black line). In Case 3D the shear stiffness was increased by a factor of 10 compared to Case 2D i.e. $F_{sh}(\theta) = \theta$; all other mechanical properties remained unchanged. The full field shear angle prediction is shown in Fig. 8g–i and shows a return towards ideal kinematics, similar to the full field shear angle measurements obtained recently using digital image correlation e.g. [61]. Shear angle predictions at the centre of Region A are again plotted in Fig. 9 (blue line) and show an intermediate result between that of Case 1D and 2D, leading to the conclusion that the kinematics of in-plane fabric shear are governed, not purely by the in-plane bending stiffness of the sheet but rather, by the ratio between the shear stiffness and the in-plane bending stiffness of the fabric (assuming a relatively high tensile stiffness along the fibre directions). The axial force prediction from Case 2D is also plotted in Fig. 10a versus both the theoretical shear angle prediction of Eq. (21) (continuous black line) and also the shear angle predicted at the centre of Region A (green line). Due to the non-ideal shear kinematics predicted in Case 2D, the method of plotting the axial force has a large effect on the result. This is important when attempting to normalise the data (in order to find the underlying shear force versus shear angle data). Fig. 10b shows the result of normalising the axial force data of Fig. 10a using Eq. (22). The theoretical axial force prediction is normalised purely to check the accuracy of the iterative normalisation algorithm (dashed thick black line). As expected, normalising the axial force prediction of Case 1D gives a close estimate of the original input curve used in the simulation (red line). Normalising the axial force predicted in Case 2D gives a reasonable estimate of the underlying shear behaviour (the input curve) only if the axial force is plotted against the shear angle predicted at the centre of Region A (green line in Fig. 10a) for normalisation, otherwise the normalisation process can produce large error if the in-plane kinematics deviate significantly from ideal kinematics and Eq. (22) is used to find the shear angle prior to normalisation (continuous black line in Fig. 10a). The fact that a reasonable estimate can be obtained by plotting the axial force against the shear angle at the centre of the specimen, prior to normalisation, is encouraging. This suggests that normalisation theory can still play useful role in interpreting uniaxial bias extension test data, despite the occurrence of non-ideal shear kinematics.

3.4. Investigating the wrinkling response of the mutually constrained pantographic beam & membrane mesh

Wrinkles are often, but not always, observed when performing uniaxial and biaxial bias extension tests [54], see for example Fig. 7b. The specimens of Cases 1D to 3D all remained almost perfectly flat (in the x - y plane, see Fig. 7) even when sheared to very high shear angles ($>80^\circ$). The final 3 simulations of this investigation examine the ability of the modelling approach in predicting realistic out-of-plane wrinkles and explore the interaction of shear stiffness, in-plane flexural stiffness and out-of-plane flexural stiffness, in creating wrinkles. In Case 4D, all parameters remained the same as Case 3D, though here a more realistic shear force versus shear angle behaviour was introduced (see Table 5 for polynomial coefficients). Fig. 11a and 11d show the result; a realistic looking wrinkle is predicted. The colour legend of Fig. 11 gives the out-of-plane displacement (in m). In Case 5D (see Fig. 11b), the out-of-plane bending stiffness was doubled, while in Case 6D (see Fig. 11c), the in-plane bending stiffness, rather than the out-of-plane bending stiffness, was doubled; all other parameters in Cases 5D and 6D were unchanged from Case 4D. The result of these

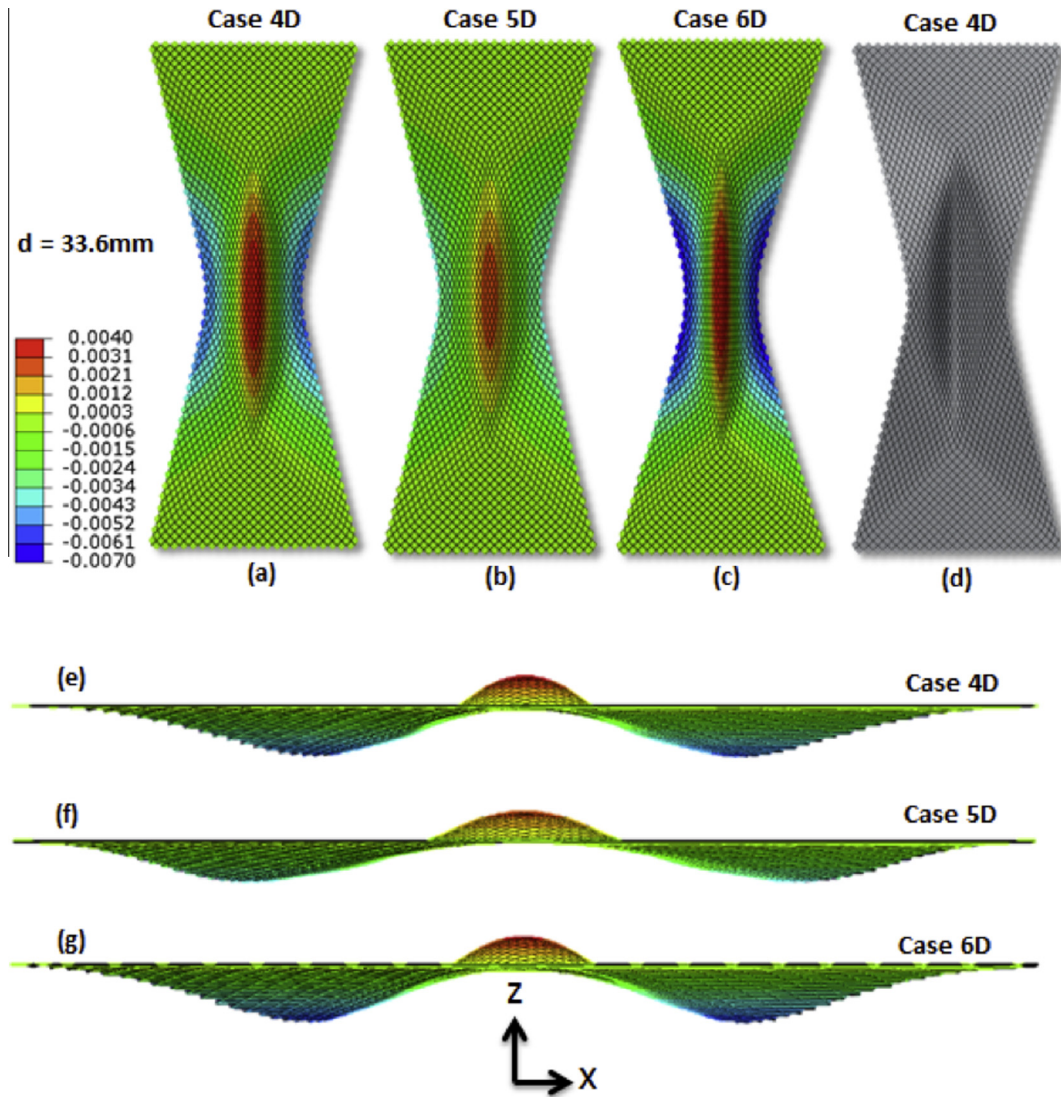


Fig. 11. (a–c) View orthogonal to x - y plane of out-of-plane displacement for simulations 4D–6D, colour legend gives displacement in (m), (d) Case 4D without colour mapping for convenient comparison with Fig. 7c, (e–g) view orthogonal to x - z plane for simulations 4D–6D showing alternative perspective of out-of-plane wrinkle. (For interpretation of the references to colour in this figure legend, the reader is referred to the web version of this article.)

changes was to delay and suppress the development of the wrinkle in Case 5D (see Fig. 11b), and accelerate and promote the development of the wrinkle in Case 6D (see Fig. 11c). An alternative perspective of these 3 simulations, in the x - z plane, is provided in Fig. 11e–g in order to more clearly visualise the form of the wrinkles. Evidently, increasing the out-of-plane bending stiffness should mitigate wrinkling and so the behaviour of Case 5D is intuitive. The result of Case 6D is less obvious but can be understood as follows; for any given displacement, d , increasing the in-plane bending stiffness concentrates and intensifies shear deformations towards the centre of Region A (as shown in Case 2D), this in turn creates larger shear stresses and therefore creates larger compressive stress across the width of the sample [38]. This results in earlier wrinkling of the test specimen with increasing in-plane bending stiffness (all other parameters remaining constant).

4. Conclusions

A modelling technique has been developed to capture the comprehensive forming mechanics of biaxial engineering fabrics. The

method is significant in that it facilitates modelling of most of the main macro-scale mechanical properties of the fabric including: the tensile properties along the two fibre directions, the (trellis) shear resistance of the sheet, the out-of-plane flexural modulus of the sheet and the in-plane flexural modulus of the sheet. In so doing, the method allows improved accuracy in predicting both the in-plane shear kinematics and the wrinkling behaviour of engineering fabrics. Experience from this investigation (and also from complex forming simulations not yet reported) suggests that the method is robust, more-so (i.e. less prone convergence issues, excessive element distortions and failed runs) than the mutually constrained truss and membrane approach used in [20]. Despite the advantages of the approach, the method is not without disadvantages; for example, the need for a bespoke mesh generator is cumbersome and makes automated iteration of simulations during optimisation and mesh sensitivity studies more challenging [22], likewise, adaptive meshing is prohibited and so developing a shell element based on a generalised continuum mechanics formulation (e.g. second order gradient theory) that can accommodate all the fundamental mechanical properties incorporated using the current approach (such as bending moduli

Table A1

Angular deflection, geometric and material parameters used in implicit simulations, results are plotted in Fig. 5. The data are organised in order of increasing angular deflection to allow easy identification of the points in Fig. 5.

Case number	Angular deflection (°)	Strip length L (mm)	Thickness h (mm)	Youngs modulus E (GPa)	Poissons ratio (–)	Density (kg m ⁻³)	Areal weight p (N m ⁻²)
1B	0.153507804	90	0.1	200	0.05	500	0.4905
2B	1.179470895	360	1	200	0.05	6000	58.86
3B	1.225887122	90	0.1	200	0.05	4000	3.924
4B	1.842307634	360	0.8	200	0.05	6000	47.088
5B	3.22884801	120	0.3	20	0.05	4000	11.772
6B	4.887146128	90	0.05	200	0.05	4000	1.962
7B	4.894480088	360	0.2	200	0.05	1000	1.962
8B	13.22576114	180	0.06	200	0.05	2000	1.1772
9B	18.49928489	360	0.1	200	0.05	1000	0.981
10B	24.20419134	180	0.08	200	0.05	7000	5.4936
11B	26.10867982	360	0.2	200	0.05	6000	11.772
12B	28.07555319	120	0.03	200	0.05	4000	1.1772
13B	28.08336455	120	0.3	2	0.05	4000	11.772
14B	29.78328309	360	0.075	200	0.05	1000	0.73575
15B	37.06050315	180	0.06	200	0.01	7000	4.1202
16B	39.30321424	360	0.15	200	0.05	6000	8.829
17B	44.39296137	120	0.3	0.1	0.05	400	1.1772
18B	44.39376649	120	0.3	1	0.05	4000	11.772
19B	49.01232305	360	0.05	200	0.05	1000	0.4905
20B	56.05523313	180	0.04	200	0.05	7000	2.7468

that convect with the fibre directions) would be a very worthwhile goal. Nevertheless, the investigation of Section 3.3 has for the first time served to elucidate the combined influence that the shear stiffness, in-plane bending stiffness and out-of-plane bending stiffness exert on the generation and growth of out-of-plane wrinkles. Indeed, because many of the fundamental mechanical properties of an engineering fabric have been shown to influence wrinkle growth during a uniaxial bias extension test, it can be concluded that careful modelling of each of these properties is required if accurate prediction of such wrinkles is to be achieved. Consequently, prediction of wrinkling behaviour in a uniaxial bias extension tests can now be regarded as one of the most demanding evaluation criteria in judging the accuracy of an engineering fabric forming model. Future work will aim to characterise such wrinkling behaviour in actual fabrics and the results will be used to assess the accuracy of the fabric forming model before employing the latter in complex forming simulations of actual complex forming processes.

Acknowledgment

The author acknowledges support for this work from the Engineering and Physical Sciences Research Council provided in the form of a feasibility study; part of EP/1033513/1.

Appendix A. A short note regarding the accuracy of the British Standard

It is interesting to note that when $\phi = 41.5^\circ$ (the slope recommended for the test standard – see Fig. 4b), Eq. (19) simplifies to

$$G_C = 0.124601pL_s^3 \quad (A1)$$

which is around 6% lower than the value of the prediction given by Eq. (17) at this angle. However, because the British Standard recommends use of the simplification,

$$\frac{1}{\frac{\tan\phi}{\cos(0.5\phi)}} \approx 1 \quad (A2)$$

in Eq. (17) when $\phi = 41.5^\circ$ and because this approximation itself contains an error of around 6%, the resulting equation recommended in the British Standard [49], i.e.

$$G_{Pe} = \frac{pL_s^3}{8} \quad (A3)$$

turns out to be remarkably close ($\approx 0.3\%$) to the corrected value given by Eq. (A1). In other words, Eq. (22), in the British Standard [49], requires no significant correction (for fabric materials of low Poisson's ratio) as the error in the power series solution proposed by Peirce [52] is compensated by an almost identical error in the assumption used in Eq. (A2) when the angular deflection is 41.5° (see Table A1).

References

- [1] Hsiao SW, Kikuchi N. Numerical analysis and optimal design of composite thermoforming process. *Comput. Meth. Appl. Mech. Eng.* 1999;177:1–34.
- [2] Harrison P, Curado-Correia N. Temperature and rate dependent multi-scale shear modelling of molten thermoplastic advanced composites. In: 19th International conference on composite materials, Montreal, Canada, 2013, 28 Jul–2 Aug.
- [3] Hancock SG, Potter KD. The use of kinematic drape modelling to inform the hand lay-up of complex composite components using woven reinforcements. *Composites Part A* 2006;37(3):413–22.
- [4] Charmetant A, Orliac JG, Vidal-Sallé E, Boisse P. Hyperelastic model for large deformation analyses of 3D interlock composite preforms. *Compos Sci Technol* 2012;72:1352–60.
- [5] Sharma SB, Sutcliffe MPF. A simplified finite element model for draping of woven material. *Compos A Appl Sci Manuf* 2004;35(6):637–43.
- [6] Skordos AA, Monroy Aceves C, Sutcliffe MPF. A simplified rate dependent model of forming and wrinkling of pre-impregnated woven composites. *Composites Part A* 2007;38:1318–30.
- [7] O'Bradaigh CM, Byron Pipes R. Finite element analysis of composite sheet-forming process. *Compos Manuf* 1991;2(3):161–70.
- [8] Boisse P, Borr M, Buet K, Cherouat A. Finite element simulations of textile composite forming including the biaxial fabric behaviour. *Composites Part B* 1997;28(4):453–64.
- [9] Yu WR, Zampaloni M, Pourboghraat F, Chung K, Kang T. Analysis of flexible bending behavior of woven preform using non-orthogonal constitutive equation. *Composites Part A* 2005;36(6):839–50.
- [10] Peng X, Guo Z, Du T, Yu WR. A simple anisotropic hyperelastic constitutive model for textile fabrics with application to forming simulation. *Compos Part B Eng* 2013;52:275–81.
- [11] Sachs U, Akkerman R, Fetfatsidis K, Vidal-Sallé E, Schumacher J, Ziegmann G, et al. Characterization of the dynamic friction of woven fabrics: experimental methods and benchmark results. *Composites Part A* 2014;67:289–98.
- [12] Badel P, Gauthier S, Vidal-Sallé E, Boisse P. Rate constitutive equations for computational analyses of textile composite reinforcement mechanical behaviour during forming. *Composites Part A* 2009;40:997–1007.
- [13] Cherouat A, Bourouchaki H. Numerical tools for composite woven fabric preforming. *Adv Mater Sci Eng* 2013;18 709495.

- [14] Yu X, Cartwright B, McGuckin D, Ye L, Mai YW. Intraply shear locking in finite element analyses of woven fabric forming processes. *Composites Part A* 2006;37:790–803.
- [15] ten Thije RHW, Akkerman R. Solutions to intra-ply shear locking in finite element analyses of fibre reinforced materials. *Composites Part A* 2008;39:1167–76.
- [16] Hamila N, Boisse P. Locking in simulation of composite reinforcement deformations. Analysis and treatment. *Composites Part A* 2013;53:109–17.
- [17] Cherouat A, Billoët JL. Mechanical and numerical modelling of composite manufacturing processes deep-drawing and laying-up of thin pre-impregnated woven fabrics. *J Mater Process Technol* 2001;118(1–3):460–71.
- [18] Lin H, Wang J, Long AC, Clifford MJ, Harrison P. Predictive modelling for optimization of textile composite forming. *Compos Sci Technol* 2007;67(15–16):3242–52.
- [19] Harrison P, Yu WR, Wang J, Long AC, Clifford M. A predictive approach to simulating the forming of viscous textile composites. *Euro Finite Elem Rev* 2005;14:613–31.
- [20] Harrison P, Gomes R, Curado-Correia N. Press forming a 0/90 cross-ply advanced thermoplastic composite using the double-dome benchmark geometry. *Composites Part A* 2013;54:56–69.
- [21] Gatouillat S, Bareggi A, Vidal-Sallé E, Boisse P. Meso modelling for composite preform shaping – simulation of the loss of cohesion of the woven fibre network. *Composites Part A* 2013;54:135–44.
- [22] Chen S, Harper LT, Endrueit A, Warrior NA. Formability optimisation of fabric preforms by controlling material draw-in through in-plane constraints. *Composites Part A* 2015;76:10–9.
- [23] Ascough J, Bez HE, Bricis AM. A simple finite element model for cloth drape simulation. *Int J Clothing Sci Technol* 1996;8(3):59–74.
- [24] Ben Boubaker B, Haussy B, Ganghoffer JF. Discrete models of woven structures. Macroscopic approach. *Compos B Eng* 2007;38(4):498–505.
- [25] d'Agostino MV, Giorgio I, Greco L, Madeo A, Boisse P. Continuum and discrete models for structures including (quasi-) inextensible elasticae with a view to the design and modeling of composite reinforcements. *Int J Solids Struct* 2015;59(1):1–17.
- [26] Pickett AK, Queckbörner T, de Luca P, Haug E. An explicit finite element solution for the forming prediction of continuous fibre-reinforced thermoplastic sheets. *Compos Manuf* 1995;6(3–4):237–43.
- [27] de Luca P, Pickett AK. Numerical and experimental investigation of some press forming parameters of two fibre reinforced thermoplastics: APC2-AS4 and PEI-CETEX. *Composites Part A* 1998;29:101–10.
- [28] Yu WR, Pourboghraat F, Chung K, Zampaloni M, Kang TJ. Non-orthogonal constitutive equation for woven fabric reinforced thermoplastic composites. *Composites Part A* 2002;33(8):1095–105.
- [29] Yu WR, Harrison P, Long AC. Finite element forming simulation for non-crimp fabrics using a non-orthogonal constitutive equation. *Composites Part A* 2005;36(8):1079–93.
- [30] Boisse P, Hamila N, Vidal-Sallé E, Dumont F. Simulation of wrinkling during textile composite reinforcement forming. Influence of tensile, in-plane shear and bending stiffnesses. *Compos Sci Technol* 2011;71(5):683–92.
- [31] Yu WR, Zampaloni M, Pourboghraat F, Chung K, Kang TJ. Analysis of flexible bending behavior of woven preform using non-orthogonal constitutive equation. *Composites Part A* 2005;36(6):839–50.
- [32] Sidhu RMJS, Averill RC, Riaz M, Pourboghraat F. Finite element analysis of textile composite preform stamping. *Compos Struct* 2001;52(3–4):483–97.
- [33] Li X, Sherwood JA, Liu L, Chen J. Simulation of double dome stamping of twill woven fabric composites. In: 8th ESAFORM conference on material forming, Cluj-Napoca, Romania; 2005. p. 1003–6.
- [34] Soteropoulos D, Fetfatsidis K, Sherwood J, Langworthy J. Digital method of analyzing the bending stiffness of non-crimp fabrics. In: Proceedings of the 14th ESAFORM conference, Belfast, United Kingdom; 2011.
- [35] Fetfatsidis KA, Sherwood JA. Chapter 3: process simulations for predicting quality of composite wind turbine blades. In: Attaf Brahim, editor. Recent advances in composite materials for wind turbines blades. The World Academic Publishing Co., Ltd.; 2013. p. 41–60.
- [36] dell'Isola F, Steigmann D. A two-dimensional gradient-elasticity theory for woven fabrics. *J Elast* 2015;118:113–25.
- [37] Ferretti M, Madeo A, dell'Isola F, Boisse P. Modeling the onset of shear boundary layers in fibrous composite reinforcements by second-gradient theory. *Z Angew Math Phys* 2014;65:587–612.
- [38] Harrison P, Yu WR, Long AC. Rate dependent modelling of the forming behaviour of viscous textile composites. *Composites Part A* 2011;42(11):1719–26.
- [39] Abaqus 6.12. Abaqus analysis user's manual.
- [40] Abdiwi F, Harrison P, Koyama I, Yu WR, Long AC, Corriea N. Characterising and modelling variability of tow orientation in engineering fabrics and textile composites. *Compos Sci Technol* 2012;72(9):1034–41.
- [41] Philpot TA. *Mechanics of materials: an integrated learning system*. 2nd ed. Wiley; 2011. p. 767.
- [42] Boisse P, Gasser A, Hivet G. Analysis of fabric tensile behaviour: determination of the biaxial tension-strain surfaces and their use in forming simulations. *Composites Part A* 2001;32:1395–414.
- [43] Buet-Gautier K, Boisse P. Experimental analysis and modeling of biaxial mechanical behavior of woven composite reinforcements. *Exp Mech* 2001;41(3):260–9.
- [44] Potluri P, Thammandra VS. Influence of uniaxial and biaxial tension on meso-scale geometry and strain fields in a woven composite. *Compos Struct* 2007;77(3):405–18.
- [45] Chen Y, Zhao T, Turner B. A new computerized data acquisition and analysis system for KES-FB instruments. *Text Res J* 2001;71(9):767–70.
- [46] Margossian A, Bel S, Hinterhoelzl R. Bending characterisation of a molten unidirectional carbon fibre reinforced thermoplastic composite using a Dynamic Mechanical Analysis system. *Composites Part A* 2015 [Available online June, 2015].
- [47] de Bilbao E, Soulat D, Hivet G, Gasser A. Experimental study of bending behaviour of reinforcements. *Exp Mech* 2010;50:333–51.
- [48] Lomov SV, Verpoest I, Barbuski M, Laperre J. Carbon composites based on multi-axial multiply stitched preforms. Part 2. KES-F characterisation of the deformability of the preforms at low loads. *Composites Part A* 2003;34(4):359–70.
- [49] British Standard. Textiles—test methods for nonwovens—Part 7: Determination of bending length, BS EN ISO 9073-7; 1998.
- [50] Lammens N, Kersemans M, Luyckx G, Van Paepegem W, Degrieck J. Improved accuracy in the determination of flexural rigidity of textile fabrics by the Peirce cantilever test. (ASTM D1388). *Text Res J* 2014;84(12):1307–14.
- [51] Plaut RH. Formulas to determine fabric bending rigidity from simple tests. *Text Res J* 2015;85(8):884–94.
- [52] Peirce FT. 26—the “handle” of cloth as a measurable quantity. *J Textil Inst Trans* 1930;21:T377–416.
- [53] Larberg Y, Åkermo M. In-plane deformation of multi-layered unidirectional thermoset prepreg – modelling and experimental verification. *Composites Part A* 2014;56:203–12.
- [54] Harrison P, Abdiwi F, Guo Z, Potluri P, Yu WR. Characterising the shear-tension coupling and wrinkling behaviour of woven engineering fabrics. *Composites Part A* 2012;43(6):903–14.
- [55] dell'Isola F, Giorgio I, Andrea U. Elastic pantographic 2D lattices: a numerical analysis on the static response and wave propagation. *Proc Estonian Acad Sci* 2015;64(3):219–25.
- [56] Harrison P, Wiggers J, Long AC. Normalisation of shear test data for rate-independent compressible fabrics. *J Compos Mater* 2008;42(22):2315–44.
- [57] Hivet G, Duong Ahn Vu. A contribution to the analysis of the intrinsic shear behaviour of fabrics. *J Compos Mater* 2011;45(6):695–717.
- [58] Harrison P, Hartel F. Correction to 'Evaluation of normalisation methods for uniaxial bias extension tests on engineering fabrics'. *Composites Part A* 2015 [accepted Oct 2015].
- [59] Hartel F, Harrison P. Evaluation of normalisation methods for uniaxial bias extension tests on engineering fabrics. *Composites Part A* 2014;37:61–9.
- [60] Potter K. Bias extension measurements on cross-ply unidirectional prepreg. *Compos Part A* 2002;33:63–73.
- [61] Pazmino J, Mathieu S, Carvelli V, Boisse P, Lomov SV. Numerical modelling of forming of a non-crimp 3D orthogonal weave E-glass composite reinforcement. *Compos A Appl Sci Manuf* 2015;72:207–18.